Optics Letters

Toroidal dipole resonances enhanced second-harmonic generation with shallow etching of lithium niobate metasurface

Wenyao Chang,[1,2] Jianmei Li,[2] Cai Luo,[1,2] Zirui Guo,[2] Shiwei Cao,[1,2] Ziyi Fu,[1,2] Ruixuan Zheng,[1,3,4] Xin Huang,[1,3] Baoli Liu,[1,3] Haifang Yang,[1] Baogang Quan,[1,3,5] Shibing Tian,[1,3] Aizi Jin,[1] Yang Guo,[1,3,*] and Changzhi Gu[1,3]

[1]Beijing National Laboratory for Condensed Matter Physics, Institute of Physics, Chinese Academy of Sciences, Beijing 100190, China
[2]Key Laboratory for Microstructural Material Physics of Hebei Province, School of Science, Yanshan University, Qinhuangdao 066004, China
[3]School of Physical Sciences, CAS Key Laboratory of Vacuum Physics, University of Chinese Academy of Sciences, Beijing 100190, China
[4]Department of Physics, The University of Hong Kong, Hong Kong SAR 999077, China
[5]Songshan Lake Material Laboratory, Guangdong 523808, China
*yangguo@iphy.ac.cn

Received 18 November 2024; revised 12 December 2024; accepted 16 December 2024; posted 17 December 2024; published 13 January 2025

Lithium niobate ($LiNbO_3$) has shown great potential for applications in nonlinear metasurfaces, thanks to its large second-order nonlinear coefficients and high integration capabilities. Optical resonances play a crucial role in further enhancing the nonlinear optical responses of $LiNbO_3$ metasurfaces (LNMS). In this study, both numerically and experimentally, we designed and fabricated a metasurface structure that supports toroidal dipole (TD) resonance to enhance second-harmonic generation (SHG). This structure, which consists of an array of shallow-etched square columns on a continuous thin film, intensifies the SHG signal at 400 nm within the $LiNbO_3$ film by means of strong local field confinement. Experimental results indicate that this signal is ten times stronger compared to that of lithium niobate on insulator (LNOI). These findings emphasize the potential of TD resonance in enhancing the performance of $LiNbO_3$ in integrated nonlinear nanophotonic applications.

https://doi.org/10.1364/OL.548072

Lithium niobate ($LiNbO_3$) is a well-known material endowed with robust nonlinear optical properties [1–5]. When fabricated into metasurfaces, these nonlinear effects can be substantially enhanced due to the strong light–matter interactions [6–12] via local electromagnetic resonance couplings. In the past, a variety of metasurface structures, including square-column structures [13], circular-hole structures [14,15], and grating structures [16], have been utilized to explore the enhanced nonlinear effects in $LiNbO_3$ materials. Among these studies, the majority have focused on traditional electromagnetic resonance modes aiming at enhancing the interaction between light and matter. However, toroidal multipoles represent a unique concept that is not part of the standard multipole expansion [17]. They constitute the third independent family of elementary electromagnetic sources, rather than just another form of multipole expansion or a high-order correction of traditional electric and magnetic multipoles [18]. This provides novel approaches to modulate the nonlinear properties of $LiNbO_3$. Compared with electric dipoles (EDs) and magnetic dipoles (MDs), toroidal dipole (TD) resonances can be highly concentrated [17,19,20], which theoretically leads to a reduction in radiation loss [18]. Moreover, TD resonances exhibit strong electromagnetic field localization, high sensitivity to environmental changes, and high Q-factor line shapes [21–23]. Integrating TD resonances into $LiNbO_3$ metasurfaces (LNMS) has the potential to significantly enhance their optical properties, thus highlighting the importance of $LiNbO_3$ nonlinear metasurfaces in the development of advanced nanophotonic devices.

On the other hand, given that $LiNbO_3$ is chemically inert, several challenges exist in the fabrication of lithium niobate metasurfaces [24]. Firstly, the issue of non-vertical sidewalls is a cause for concern [25–28]. As the etching depth of lithium niobate increases, reactive ions encounter difficulties in penetrating the gaps between structures. This results in incomplete etching and the formation of non-vertical sidewalls. Secondly, high surface roughness is another problem [29]. When using inductively coupled plasma (ICP) etching [30], factors such as non-uniform energy distribution or local charge accumulation can lead to uneven ion bombardment. Consequently, different etching rates occur in different areas, leading to a rough surface. Fortunately, reducing the thickness of $LiNbO_3$ resonators to hundreds of nanometers can partially resolve this issue due to shallow etching. Regarding the sidewall issue, during shallow etching, the shorter distance that reactive ions need to travel allows them to enter the gaps between unit structures more easily [31,32]. In terms of surface roughness, the etching rate can be controlled by reducing the temperature during the shallow etching [33,34]. This slows down the movement and reaction rate of reactive

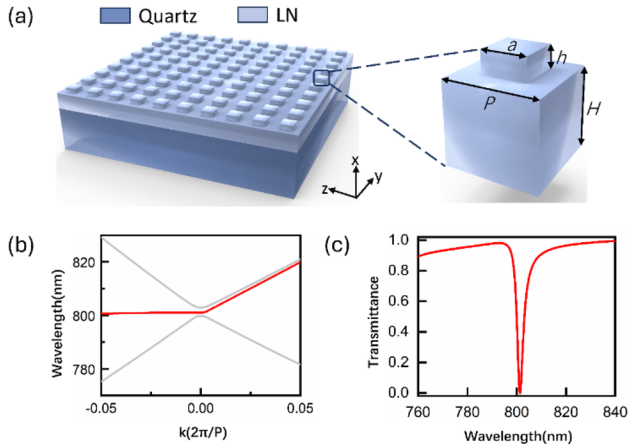

Fig. 1. Linear optical properties of metasurfaces. (a) Schematic illustration of the LNMS structure. The parameter for the LNMS is $P = 478$ nm, $a = 230$ nm, $h = 100$ nm, and $H = 360$ nm. (b) Calculated band diagram of the metasurface. The resonance wavelength is located at 800 nm (indicated by the red line). (c) Calculated linear transmission spectra of the metasurface.

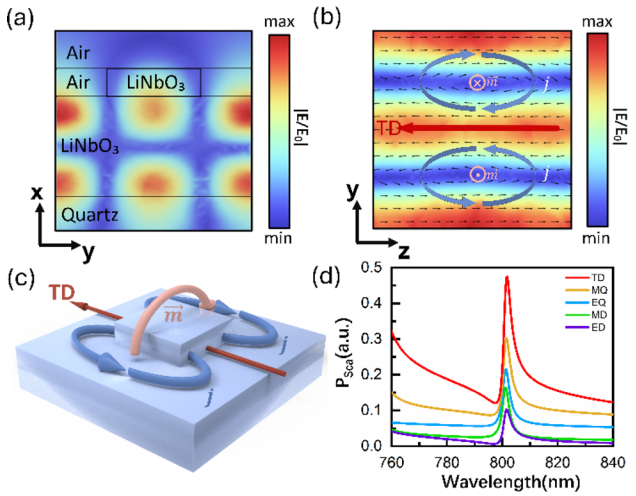

Fig. 2. Electric field distributions and the working principle of the TD resonance mode. (a)–(b) Near-field distributions of the local electric field ($|E/E_0|$) in the x–y plane (a) and y–z plane (b) at the resonance of the LNSM; the black arrows represent the distribution of polarization currents. (c) Schematic of the designed meta-atom and formation of toroidal dipole modes. (d) Numerically calculated spectra of the scattered power and corresponding multipoles' contributions from five different multipoles.

ions, thereby enhancing the etching uniformity and avoiding the surface roughness caused by local over- or under-reaction.

This paper numerically and experimentally demonstrates an efficient and robust approach to achieve second-harmonic generation (SHG) enhancement based on an all-dielectric metasurface. The metasurface is composed of patterned $LiNbO_3$ square columns and a continuous underlying $LiNbO_3$ thin film, supporting TD resonance induced by the head-to-tail arrangement of MD. For the first time, the TD resonance localizes the pump fields within the high refractive index $LiNbO_3$ film, leading to a ten-fold increase in SHG from $LiNbO_3$. In addition, the ICP dry etching process is capable of meeting the requirements for large-area metasurface uniform preparation, controllable etch thickness, steep sidewalls, and smooth structures. This study presents a novel approach for the etching of $LiNbO_3$, enabling multifunctional integration and providing a solution for experimental preparation in micro-/nano- machining. Our work not only breaks the new ground for developing efficient SHG to be achieved at a low pump power but also expands the application of all-dielectric metasurfaces.

Figure 1(a) shows the schematic of the LNMS. The sample consists of a continuous bottom layer with a thickness of $H = 360$ nm x-cut $LiNbO_3$ thin film on an insulating substrate, capped by a LNMS. For the metasurface building block, we select a square-shaped nanoresonator, with dimensions of $a \times a$ square ($a = 230$ nm) and a height of $h = 100$ nm. The array of meta-atoms is arranged in a square lattice with an array pitch of $P = 478$ nm. Figure 1(b) illustrates the calculated band diagram of the metasurface (see Section S6 in Supplement 1 for more details), with the resonance mode located at the center of the first Brillouin zone (indicated by the red line). By carefully designing the structure's geometry parameters, the resonant mode can be adjusted to the desired fundamental wavelength (FW) of 800 nm. The incident light was normally TE-polarized, with the electric field parallel to the z axis in Cartesian coordinates. The linear transmission spectra of the metasurface, depicted in Fig. 1(c), exhibit a narrow resonant dip at 800 nm with a full width at half maximum (FWHM) of 3.2 nm.

The structure we have designed supports the guided mode resonance [35,36]. In this structure, the electric field of the resonance mode is confined within the slab, as shown in Fig. 2(a). According to previous studies, the guided mode resonances can be analyzed as the superposition of different electric and magnetic multipoles [35,36]. For example, the resonant mode in Fig. 2(b) exhibits an electric field distribution with a TD nature polarizing along the z axis. The blue arrows represent two opposite direction circular current distributions j, one clockwise and the other counterclockwise. Indeed, the formation of the head-to-tail arrangement of magnetic dipoles is a strong signature of the TD excitation. More intuitively, Fig. 2(c) shows the TD diagram supported by the structure. The maximum field intensity occurs at a height of 290 nm above the substrate in the yz section. Thus, the TD resonance supported by a dielectric metasurface effectively traps the pump fields within the $LiNbO_3$ film. According to the previous studies [37–39], strong optical electric field confinement is crucial for improving nonlinear responses in nanophotonic structures.

In Fig. 2(d), the scattering power of multiple multipoles was calculated by determining the induced current densities in the nanostructures, following the approach described in Section S1 in Supplement 1. Several peaks are observed at resonant wavelengths, including ED, MD, TD, electric quadrupole (EQ), and magnetic quadrupole (MQ). In particular, the most intense and robust TD resonance is the dominant multipole in relation to other moments, observed at a wavelength of 800 nm within the 760 nm–840 nm range, which is consistent with the TD nature of the electric field distribution shown in Fig. 2(a). Furthermore, the field enhancement ($|E/E_0|$) inside the $LiNbO_3$ reaches up to ten times in both Figs. 2(a) and 2(b), thus confirming the field enhancement capability of the TD resonance mode.

To verify our proposal experimentally, we fabricated the $LiNbO_3$ metasurfaces on the lithium niobate on insulator (LNOI)

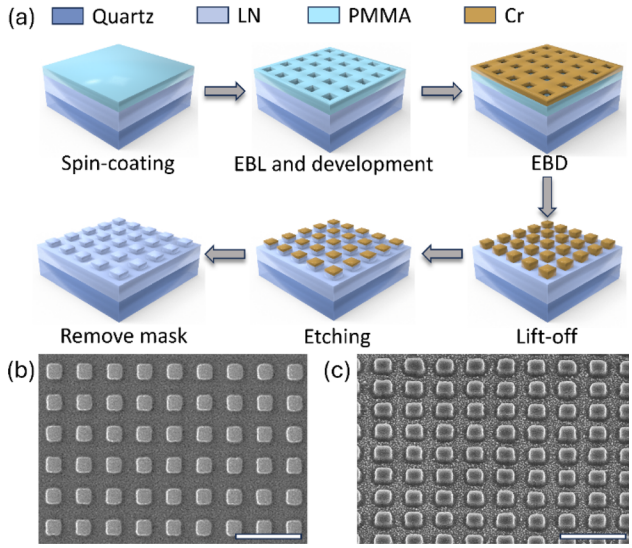

Fig. 3. Nanofabrication process and sample characterization. (a) Schematic of the fabrication steps involved in achieving a shallowly etched LNMS. (b)–(c) Top (b) and tilt (c) view SEM images of the fabricated metasurface. The scale bar is 1 μm. The dimension of our metasurface is 1 mm × 1 mm.

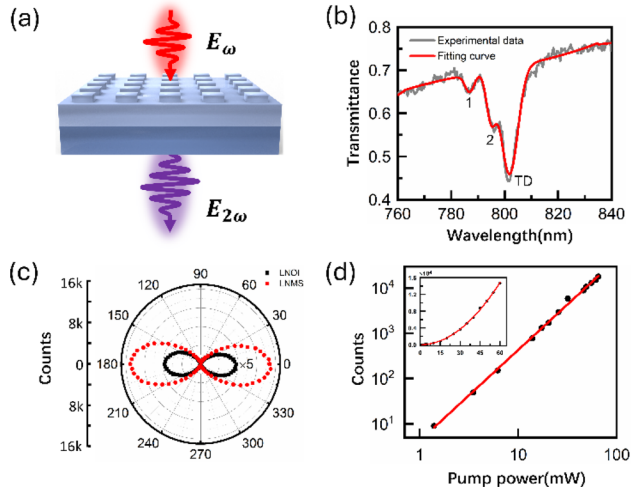

Fig. 4. Nonlinear optical properties of metasurfaces. (a) Artist's view of SHG enhancement by an all-dielectric metasurface: the pump laser pulses and the emitted SH polarized along the optical axis (z axis) of an x-cut $LiNbO_3$. (b) Transmission spectra of LNMS. The gray line denotes the experimental data and the red line represents fit results. (c) Dependence of the SHG intensity on the pump polarization directions of LNMS (red dots) and LNOI (black squares). (d) Log–plot power dependence of the SH signal with a pump power ranging from 1 mW to 65 mW, and the fitting slope is 2.00591. The SHG counts indicate a squared relationship with the increasing excited average pump power (as shown in the left inset).

by the electron-beam lithography (EBL) technique. A commercially available x-cut lithium niobate on insulator (LNOI) wafer was fabricated by ion slicing [40,41]. In our work, the $LiNbO_3$ thin film had a thickness of 460 nm and was bonded to a SiO_2 layer of 2 μm thick, which was grown on a quartz substrate (NANOLN, Jinan Jingzheng Electronics Co., Ltd., Jinan, Shandong, China). The fabrication process, outlined in Fig. 3(a), includes steps such as polymethyl methacrylate (PMMA) spin-coating, electron-beam lithography patterning, chromium mask fabrication, and inductively coupled plasma etching (see Section S5 in Supplement 1 for more details). Shown in Figs. 3(b) and 3(c), the $LiNbO_3$ metasurfaces, measuring 1 mm × 1 mm, exhibit high quality with vertical sidewalls and uniform surfaces, as confirmed by the scanning electron microscope (SEM) images, with steep sidewall and decent surface morphology.

Figure 4(a) illustrates the schematic of enhancing SHG by the all-dielectric metasurfaces when excited by near-infrared (NIR) femtosecond laser pulses. To guarantee that the orientation with the largest nonlinear coefficient (d_{33}) is in-plane, we choose the x-cut $LiNbO_3$. The electric field polarization of the pump light aligns with the optic axis of $LiNbO_3$ (z axis). Figure 4(b) illustrates the transmittance spectrum of the LNMS. The gray line represents the experimental data, whereas the red line indicates the result of the three-peak fitting analysis. The peak at 800 nm in Fig. 4(b) aligns with the theoretical transmission spectrum and is attributed to the TD resonance. The oscillatory characteristics of peak 1 and peak 2 observed in the transmission measurement are likely due to multiple resonances or Fabry–Perot oscillations [42–44] and may also be due to the interference effect of the thin film caused by the substrate of the sample [45]. Our metasurface is fabricated on a quartz substrate with a thickness of 500 μm, resulting in weak oscillation in the transmission measurements. The measured resonances are broader compared with the calculated spectra (see Fig. 1(c)). The theoretical simulation Q-factor is 262. By fitting the experimental data of transmission spectrum using Gaussian curves, the Q-factor of TD resonance is extracted as 104. The deviations between the experiments and simulations may be attributed to the fabrication imperfections that are difficult to account for in the simulations. In addition, the incident light was focused onto the samples in experiments, while a plane wave source was used in the simulations.

The SHG spectra of the LNMS and LNOI were measured with our homemade nonlinear optical measurement system, which was excited by NIR laser pulses with a central wavelength of 800 nm, a repetition rate of 1 kHz, and a duration of 120 fs (see Fig. S2 in Supplement 1). In Fig. 4(c), it is evident that LNMS significantly increases the SH signal in comparison to LNOI. The SH intensity of the LNMS is approximately ten times larger than that of the LNOI, indicating the critical role of TD resonance in enhancing SHG. Additionally, we simulate the SHG conversion efficiency from the LNMS sample, as illustrated in Fig. S3 in Supplement 1. At the resonance wavelength of 800 nm, the LNMS demonstrates a conversion efficiency that is two orders of magnitude higher than that of LNOI. The deviation between the experiment and the simulation may come from the experimental Q-factor of the resonant mode smaller than the simulated ones. The polarization pattern of SHG is mainly determined by the polarization of the incident light and the nonlinear coefficient of the material, which presents an eight-shaped pattern (see Section S7 in Supplement 1 for more details). Figure 4(d) shows the SHG intensity from the LNMS as a function of the pump power ranging from 1 mW to 65 mW, with a linear fit shown in a log–log plot. The SHG counts showed a quadratic relationship with an increasing average pump power, as illustrated in the left inset. The log plot demonstrated a linear dependence with a slope of approximately 2, indicating a second-order nonlinear process.

In conclusion, we have successfully designed and fabricated high-quality all-dielectric LNMS on the LNOI platform, thereby achieving SHG enhancement. Our experimental findings indicate that the SH intensity has been enhanced by up to a factor of 10 compared to that of unpatterned LNOI. The enhancement of SHG is attributed to the TD resonance, which significantly confines the pump electric fields within the $LiNbO_3$ films. The precise control of nanoscale structures in $LiNbO_3$ was achieved through the use of multiple gas compositions and ICP etching techniques. This approach enabled high selectivity and etching rates, resulting in the optimal steepness of the structures in our study. Additionally, we can modulate the resonant wavelength for SHG by fine-tuning the geometric unit parameters of the metasurfaces, such as length, period, and thickness. This adjustment allows for the application of SHG across a broader spectrum of wavelengths, encompassing both the visible and ultraviolet regions. Our research expands the potential for the extensive application of $LiNbO_3$ in the field of nonlinear integrated nanophotonics.

Funding. National Natural Science Foundation of China (92265110, 62174179, 62204259, 12332002); National Key Research and Development Program of China (2024YFA1207700, 2022YFA1204100, 2021YFA1400700); Strategic Priority Research Program of the Chinese Academy of Sciences (XDB33020200).

Acknowledgments. This work was also supported by the Micro/nano Fabrication Laboratory of Synergetic Extreme Condition User Facility (SECUF).

Disclosures. The authors declare no conflicts of interest.

Data availability. Data underlying the results presented in this paper are not publicly available at this time but may be obtained from the authors upon reasonable request.

Supplemental document. See Supplement 1 for supporting content.

REFERENCES

1. C. Wang, M. Zhang, X. Chen, *et al.*, Nature **562**, 101 (2018).
2. R.-R. Xie, G.-Q. Li, F. Chen, *et al.*, Adv. Opt. Mater. **9**, 2100539 (2021).
3. R. S. Weis and T. K. Gaylord, Appl. Phys. A **37**, 191 (1985).
4. Y. Zheng, Z. Fang, S. Liu, *et al.*, Phys. Rev. Lett. **122**, 253902 (2019).
5. B. Gao, M. Ren, W. Wu, *et al.*, Laser Photonics Rev. **13**, 1800312 (2019).
6. M. F. Limonov, M. V. Rybin, A. N. Poddubny, *et al.*, Nat. Photonics **11**, 543 (2017).
7. P. P. Vabishchevich, S. Liu, M. B. Sinclair, *et al.*, ACS Photonics **5**, 1685 (2018).
8. F. Timpu, J. Sendra, C. Renaut, *et al.*, ACS Photonics **6**, 545 (2019).
9. M. Timofeeva, L. Lang, F. Timpu, *et al.*, Nano Lett. **18**, 3695 (2018).
10. Y. Li, Z. Huang, Z. Sui, *et al.*, Nanophotonics **9**, 3575 (2020).
11. C. W. Hsu, B. Zhen, A. D. Stone, *et al.*, Nat. Rev. Mater. **1**, 16048 (2016).
12. A. P. Anthur, H. Zhang, R. Paniagua-Dominguez, *et al.*, Nano Lett. **20**, 8745 (2020).
13. A. Fedotova, M. Younesi, J. Sautter, *et al.*, Nano Lett. **20**, 8608 (2020).
14. L. Qu, L. Bai, C. Jin, *et al.*, Nano Lett. **22**, 9652 (2022).
15. J. Li, W. Chang, Z. Guo, *et al.*, Appl. Phys. Lett. **124**, 131702 (2024).
16. Z. Huang, M. Wang, Y. Li, *et al.*, Nanotechnology **32**, 325207 (2021).
17. T. Kaelberer, V. A. Fedotov, N. Papasimakis, *et al.*, Science **330**, 1510 (2010).
18. N. Papasimakis, V. A. Fedotov, V. Savinov, *et al.*, Nat. Mater. **15**, 263 (2016).
19. A. Ahmadivand, B. Gerislioglu, R. Ahuja, *et al.*, Laser Photonics Rev. **14**, 1900326 (2020).
20. M. Gupta and R. Singh, Rev. Phys. **5**, 100040 (2020).
21. Y. Fan, Z. Wei, H. Li, *et al.*, Phys. Rev. B **87**, 115417 (2013).
22. M. Gupta, V. Savinov, N. Xu, *et al.*, Adv. Mater. **28**, 8206 (2016).
23. C. Cui, S. Yuan, X. Qiu, *et al.*, Nanoscale **11**, 14446 (2019).
24. D. Zhu, L. Shao, M. Yu, *et al.*, Adv. Opt. Photonics **13**, 242 (2021).
25. Y. Qi and Y. Li, Nanophotonics **9**, 1287 (2020).
26. H. Weigand, V. V. Vogler-Neuling, M. R. Escalé, *et al.*, ACS Photonics **8**, 3004 (2021).
27. J. Ma, F. Xie, W. Chen, *et al.*, Laser Photonics Rev. **15**, 2000521 (2021).
28. L. Carletti, A. Zilli, F. Moia, *et al.*, ACS Photonics **8**, 731 (2021).
29. A. Guarino, G. Poberaj, D. Rezzonico, *et al.*, Nat. Photonics **1**, 407 (2007).
30. S. J. Hill, *Inductively Coupled Plasma Spectrometry and Its Applications* (John Wiley & Sons, 2006).
31. J. Lin, A. Leven, N. G. Weimann, *et al.*, J. Vac. Sci. Technol., B:Nanotechnol. Microelectron.:Mater., Process., Meas., Phenom. **22**, 510 (2004).
32. S. Guilet, S. Bouchoule, C. Jany, *et al.*, J. Vac. Sci. Technol., B:Nanotechnol. Microelectron.:Mater., Process., Meas., Phenom. **24**, 2381 (2006).
33. A. Wieczorek, V. Djara, F. H. Peters, *et al.*, J. Vac. Sci. Technol., B:Nanotechnol. Microelectron.:Mater., Process., Meas., Phenom. **30**, 051208 (2012).
34. H.-C. Lee, B. H. Seo, D.-C. Kwon, *et al.*, Appl. Phys. Lett. **110**, 014106 (2017).
35. I. A. M. Al-Ani, K. As'Ham, L. Huang, *et al.*, Adv. Opt. Mater. **10**, 2101120 (2022).
36. Z. Zheng, D. Smirnova, G. Sanderson, *et al.*, Light: Sci. Appl. **13**, 249 (2024).
37. H. Liu, C. Guo, G. Vampa, *et al.*, Nat. Phys. **14**, 1006 (2018).
38. G. Grinblat, Y. Li, M. P. Nielsen, *et al.*, Nano Lett. **16**, 4635 (2016).
39. S. Liu, M. B. Sinclair, S. Saravi, *et al.*, Nano Lett. **16**, 5426 (2016).
40. X. Ye, S. Liu, Y. Chen, *et al.*, Opt. Lett. **45**, 523 (2020).
41. R. Wu, M. Wang, J. Xu, *et al.*, Nanomaterials **8**, 910 (2018).
42. H. Ou, F. Lu, Z. Xu, *et al.*, Nanomaterials **10**, 1038 (2020).
43. M. Chen, L. Singh, N. Xu, *et al.*, Opt. Express **25**, 14089 (2017).
44. R. Sengupta, H. Khand, and G. Sarusi, ACS Appl. Mater. Interfaces **16**, 45107 (2024).
45. P. Ren, Z. Huang, S. Luo, *et al.*, Nanophotonics **13**, 3449 (2024).